Nanoscale

PAPER

View Article Online
View Journal | View Issue

Cite this: *Nanoscale*, 2022, **14**, 7250

Manipulation of the crystalline phase diagram of hydrogen through nanoscale confinement effects in porous carbons†

Lui R. Terry, *[a] Stephane Rols, [b] Mi Tian, [c] Ivan da Silva, [d] Simon J. Bending [e] and Valeska P. Ting *[a]

Condensed phases of molecular hydrogen (H_2) are highly desired for clean energy applications ranging from hydrogen storage to nuclear fusion and superconductive energy storage. However, in bulk hydrogen, such dense phases typically only form at exceedingly low temperatures or extremely high (typically hundreds of GPa) pressures. Here, confinement of H_2 within nanoporous materials is shown to significantly manipulate the hydrogen phase diagram leading to preferential stabilization of unusual crystalline H_2 phases. Using pressure and temperature-dependent neutron scattering at pressures between 200–2000 bar (0.02–0.2 GPa) and temperatures between 10–77 K to map out the phase diagram of H_2 when confined inside both meso- and microporous carbons, we conclusively demonstrate the preferential stabilisation of face-centred cubic (FCC) solid *ortho*-H_2 in microporous carbons, at temperatures five times higher than would be possible in bulk H_2. Through examination of nanoconfined H_2 rotational dynamics, preferential adsorption and spin trapping of *ortho*-H_2, as well as the loss of rotational energy and severe restriction of rotational degrees of freedom caused by the unique micropore environments, are shown to result in changes to phase behaviour. This work provides a general strategy for further manipulation of the H_2 phase diagram *via* nanoconfinement effects, and for tuning of anisotropic potential through control of confining material composition and pore size. This approach could potentially provide lower energy routes to the formation and study of more exotic non-equilibrium condensed phases of hydrogen that could be useful for a wide range of energy applications.

Received 31st January 2022,
Accepted 4th April 2022

DOI: 10.1039/d2nr00587e

rsc.li/nanoscale

1. Introduction

The urgent global need for alternative and clean energy sources has driven demand for compact or condensed forms of H_2, as a sustainable, zero-carbon fuel.[1] Furthermore, the promise of room-temperature superconductivity in metallic hydrogen[2–4] has also driven interest in the creation of high-density hydrogen solids and other condensed non-equilibrium hydrogen phases. The phase diagram of H_2 is indeed rich, with eight solid phases of pure hydrogen being thought to exist,[4–11] ranging from phase I hexagonally close-packed (HCP) H_2,[5,12] metastable FCC *ortho*-H_2,[11,13] the broken symmetry phase (II)[10] all the way up to *Cmca*$\bar{1}$2 metallic hydrogen.[4] However, one of the most challenging aspects of the practical use of H_2 stems from its existence as a very low-density gas across most accessible temperatures and pressures, with the formation of solid phases requiring temperatures below 13.8 K (at 1 bar)[14] or pressures up to millions of times atmospheric pressure to form at ambient temperature.[12] The practical limitations of working at such high pressures or low temperatures make the application and study of condensed H_2 experimentally demanding, necessitating the exploration of alternative routes toward the formation of compact and condensed hydrogen phases at more accessible temperatures or pressures.

The adsorption of gases into nanoporous materials has been studied as a method of densifying gaseous hydrogen to higher gravimetric and volumetric densities.[15–17] Recently, experimental studies of H_2 adsorbed in highly microporous carbons with pore diameters <2 nm have demonstrated the formation of H_2 with solid-like characteristics at atmospheric

[a]*Department of Mechanical Engineering, University of Bristol, BS8 1TR UK. E-mail: v.ting@bristol.ac.uk, lt7006@bristol.ac.uk*
[b]*Institut Laue-Langevin (ILL), Grenoble, France*
[c]*College of Engineering, Mathematics and Physical Sciences, University of Exeter, EX4 4QF, UK*
[d]*ISIS Neutron Source, Rutherford Appleton Laboratory, Harwell Oxford, Didcot OX11 0QX, UK*
[e]*Department of Physics, University of Bath, Bath BA2 7AY, UK*

† Electronic supplementary information (ESI) available: EDX, ICP-OES and pore characteristics of the activated carbons, neutron and X-ray powder diffraction data, unit cell dimensions, inelastic neutron scattering peak parameters and *ortho*/*para*-H_2 distributions. See DOI: **https://doi.org/10.1039/d2nr00587e**

pressure and temperatures above hydrogen's critical temperature – conditions where, classically, bulk H_2 should be gaseous. Results have shown severely restricted mobility of molecules,[18,19] increased densities,[15,16,20,21] signature quantum rotational transitions of solid-like H_2 at temperatures up to 100 K (ref. 16 and 17) and have allowed observation of possible phase transitions[22] when pore diameters are smaller than 1 nm. If appreciable manipulation of the H_2 phase diagram can be achieved through nanoconfinement in porous materials such as these, lower energy routes to more exotic non-equilibrium condensed phases of H_2 could be identified and potentially exploited for applications such as H_2 fuel storage, superconductivity, or fusion pellets. Furthermore, such porous materials may be readily scalable, which is key for any envisaged future large-scale technological applications of solid hydrogen. Thus, a better understanding of what happens to nanoconfined H_2 is necessary to help us design and model better H_2 confinement materials for future applications.

To understand how confinement could be extended to produce and study condensed phases of hydrogen, a detailed investigation of which solid phases of H_2 form under confinement and why was conducted, using confinement inside both mesoporous (pore diameters >2 nm) and microporous (pores <2 nm in diameter) carbons. Here we used a powerful combination of variable-temperature and variable-pressure neutron diffraction and inelastic neutron scattering (INS) studies. The large neutron scattering cross-section of the hydrogen nucleus makes neutrons highly sensitive to hydrogen atoms, meaning that the structural arrangement and dynamic properties of the multiple phases of H_2 confined within a carbon nanomaterial can be easily distinguished.[23] Our results uncover considerable manipulation of the H_2 phase diagram by nanoconfinement. For the first time, the crystal structures of H_2 confined in microporous activated carbons have been revealed and the driving forces behind preferential adsorption and spin trapping of solid *ortho*-H_2, when confined in highly microporous carbon, have been identified, furthering our understanding of H_2 phase manipulation and stabilisation by nanoconfinement effects.

2. Experimental

2.1 Materials and preparation

To investigate the effects of nanoscale confinement on the crystal structures and phase diagram of H_2, two porous carbons (a microporous "TE7" carbon and a mesoporous onion like carbon, "OLC") were chosen due to their amorphous graphitic carbon frameworks of slit-shaped pores and their differing pore size distributions. TE7 is a highly microporous disordered activated carbon derived from phenolic resin, sourced from MAST Carbon International Ltd (Basingstoke, UK). OLC is a highly mesoporous activated carbon synthesised by vacuum annealing of detonation nanodiamond powder[24] and was supplied by Prof. Volker Presser (INM, Saarland University, Saarbrücken, Germany). All other chemicals used were sourced from Sigma Aldrich and used as received unless otherwise stated.

All experiments used room temperature "normal H_2" gas, comprised of a 1 : 3 equilibrium mixture of the two nuclear spin isomers of hydrogen, *para*-H_2 and *ortho*-H_2, respectively. *para*-H_2 is the ground state of H_2, whereby nuclear spins on each hydrogen atom are antisymmetric. It is characterized by an even rotational quantum number ($J = 0$) where its rotation and charge distribution are spherical/isotropic (see HCP in Fig. 1). *ortho*-H_2 is the first excited state and is therefore metastable, having symmetric nuclear spins characterized by an odd rotational quantum number ($J = 1$) where its rotations and charge distribution are anisotropic (see FCC in Fig. 1). A minimum of 99.999% purity "normal H_2" was used for all experiments.

Paramagnetic metal impurities are known to catalyse the conversion of *ortho*-H_2 to *para*-H_2. In preparation for physical characterization, all carbon materials were powdered using an agate mortar and pestle, then washed in HCl to remove any possible metal contaminants. Samples were suspended in aqueous 1 mol dm^{-3} HCl (ultra-trace analysis) at 100 mg mL^{-1}, then sonicated for 15 minutes before filtering and a second rinse with 1 M HCl. This process was then repeated with an excess of acetone (ultra-trace) followed by methanol (ultra-trace) and finally ultra-pure deionised water. Samples were completely dried at 623 K under dynamic vacuum ($P <$ 0.001 bar) for a minimum of 8 hours before any physical characterisation.

2.2 Gas sorption analysis

The specific surface area and internal pore structure of both samples were obtained from N_2 adsorption at 77 K and CO_2 adsorption at 298 K on a Micromeritics 3Flex volumetric gas sorption analyser. Samples (~120 mg) were degassed under vacuum prior to the experiment (623 K, ~8 h, 1×10^{-6} mbar). Helium was used for free-space determination following isotherm collection. N_2 and helium were supplied by Air Liquide and of a purity of 99.999%. Pore volume distribution as a function of pore width was calculated from combined CO_2 and N_2 adsorption data using the advanced combination non-local density functional theory (NL-DFT) method and an asymmetrical slit-shaped pore model. The BET surface area was calculated according to the procedure from ISO 9277 (see ESI – Table S1 and Fig. S1†).

2.3 Powder X-ray diffraction

Information on the structure of the carbons was obtained by powder X-ray diffraction (PXRD) using a Bruker D8 diffractometer (Cu Kα source, $\lambda = 1.54$ Å), with a step size of 0.05 2θ and an integration time interval of 3 seconds. Diffraction data of the silicon sample holder was background subtracted for clarity, due to the low diffraction intensities of the carbon samples (see ESI – Fig. S2†).

2.4 Neutron diffraction

Structural information on the adsorbed H_2 phase was obtained by neutron diffraction on the neutron powder diffraction

instrument, GEM, at the ISIS neutron source, Rutherford-Appleton Laboratories, UK.[25] Results obtained (**https://doi.org/10.5286/ISIS.E.RB1910448**(2019)) were calibrated and refined against a silicon standard taken prior to the experiment. TE7 and OLC samples were degassed (623 K, 1×10^{-6} mbar) prior to examination to remove adsorbed water and trace gases. Dry samples were loaded into an aluminium sample cell (diameter 0.8 cm; volume 3.5 cm^3) inside a He-filled glove box and tamped to reduce the level of interstitial voids between particulates as much as possible. The sample cell was filled and centred to ensure no free-space contribution was included in the beam. Care was taken to ensure the packing between the two samples was similar, so that differences observed in the diffraction patterns could be attributed to differences in the inner micro/mesoporosity of the samples, rather than any hydrogen in the interstitial spaces between particles. Loaded cells were leak tested under vacuum with 2 kbar He, before evacuation at room temperature for at least 1 hour to remove helium from the micropores. To decrease the diffraction signal of the aluminium sample cell, a collimator was used, reducing the beam size to 30 × 5 mm (vertical × horizontal) and removing diffraction banks 4 and 6 from use. Background measurements of the carbon samples were collected at room temperature and 77 K under vacuum for 4 hours (see ESI – Fig. S3–S5†). The background diffraction patterns (recorded under vacuum) indicated an amorphous carbon framework in both cases, with no sharp diffraction peaks and only a broad and diffuse (002) graphitic feature for OLC observed at 3.46 Å (as indicated by powder X-ray diffraction patterns – Fig. S2†).

Samples were then dosed with normal-H_2 to either 200 or 2000 bar at 77 K before temperature cycling. Neutron diffraction data were collected at 77 K for 3 hours before the samples were cooled to 10 K, after which data was collected for at least 2.5 hours at 10, 15, 25, 52 and 77 K. At 10 K, the pressure inside the cells dropped by ~3.3% due to thermal contraction. Data was collected from diffraction banks 3 & 5 of the GEM instrument for analysis due to their appropriate *d*-spacing range for H_2 (1.4–5 Å) and resolution (bank 3: $\sim 2 \times 10^{-2}$ $\Delta d/d$, bank 5: $\sim 5 \times 10^{-3}$ $\Delta d/d$). Observed diffraction peaks were indexed and treated with full Rietveld refinement using the TOPAS v6-Academic software. Relative percentages of each phase were calculated using all peaks in each diffraction pattern. Clear diffraction peaks from the aluminium sample cell could still be observed throughout the experiment (see Fig. S3– S5†).

2.5 Inelastic neutron scattering

INS spectra collected on IN4 at the Institut Laue Langevin, France used an incident neutron wavelength of 1.6 Å and a Fermi chopper speed of 15 000 rpm. This allowed measurement of a large (Q, E) scattering region (energy transfer range $E = [-75, 28$ meV], momentum transfer range $Q = [1, 7$ $Å^{-1}]$ at elastic scattering). The energy resolution at 0 meV energy transfer (elastic scattering) is 2.1 meV. Raw data were transformed into the physical observable $S(Q, E)$, often called dynamical structure factor, according to classical time-of-flight procedures, were corrected from the neutron energy dependence efficiency of the detectors and calibrated using a vanadium standard. The measurements allowed quantitative analysis of $S(Q, E)$ as a function of gas pressure. The ~5 cm^3 sample of TE7 beads was acid-washed to remove any residual metal content prior to analysis, then degassed at 623 K for 8 hours under vacuum (1×10^{-6} mbar) and loaded into a cylindrical aluminium sample can inside a dry argon glove box. Sample temperatures were regulated between 4 K and 200 K using an ancillary cryo-furnace. Samples were dosed with normal H_2 (Air Liquide, 99.999% purity) using a Hiden Isochema HTP-1 gas sorption analyser and equilibrated at 1 bar and 77 K. Pressure was recorded using a 1 bar baratron and a high-pressure (20 bar) transducer. The TE7 carbon sample was dosed with 1 bar H_2 at 77 K and left to equilibrate for 1 hour. The system was then sealed and cooled to 40 K and 4 K. INS data were collected at the appropriate temperatures and pressures over a period of two hours and were background-subtracted with degassed samples under vacuum at the corresponding temperatures and pressures over the same time period, to remove spectral contributions from the carbon support.

Rotational transitions were fitted to a set of Gaussian lines, with the full-width at half-maximum fixed to the resolution of the spectrometer at the corresponding energy transfer. The Gaussian lines in the anti-Stokes side of the spectrum were added to a background composed of a unique elastic contribution (considered as Gaussian) plus a Lorentzian function (to account for a quasielastic like background centred at zero energy transfer). On the Stokes side, the background accounted in addition for a broad recoil-like scattering which was fitted to a large gaussian shape. All Gaussian lines representing the rotational transitions were fitted simultaneously, with their centres and width being tight from one Q value to the other. Their integrated intensity was further fitted to the function:

$$S(Q) = \exp\left(-\frac{Q^2U^2}{3}\right) \times \left[j_1\left(\frac{Qa}{2}\right)\right]^2;\ a = 0.74\,\text{Å} \qquad (1)$$

to extract the mean squared displacement U^2 which accounts for H_2 translational vibrations (see ESI – Fig. S6†). Note that the value of a (the H–H interatomic distance) was fixed to 0.74 Å.

Further analysis of the quantum rotations considered a 3D hindered rotational model, the anisotropic potential term being chosen of the form

$$W = V \sin^2(\theta) \qquad (2)$$

The total Hamiltonian

$$\hat{H} = B \times J(J+1) + W \qquad (3)$$

is treated in perturbation to first order in energy. The parameters B and V were varied to give the best agreement with the data.

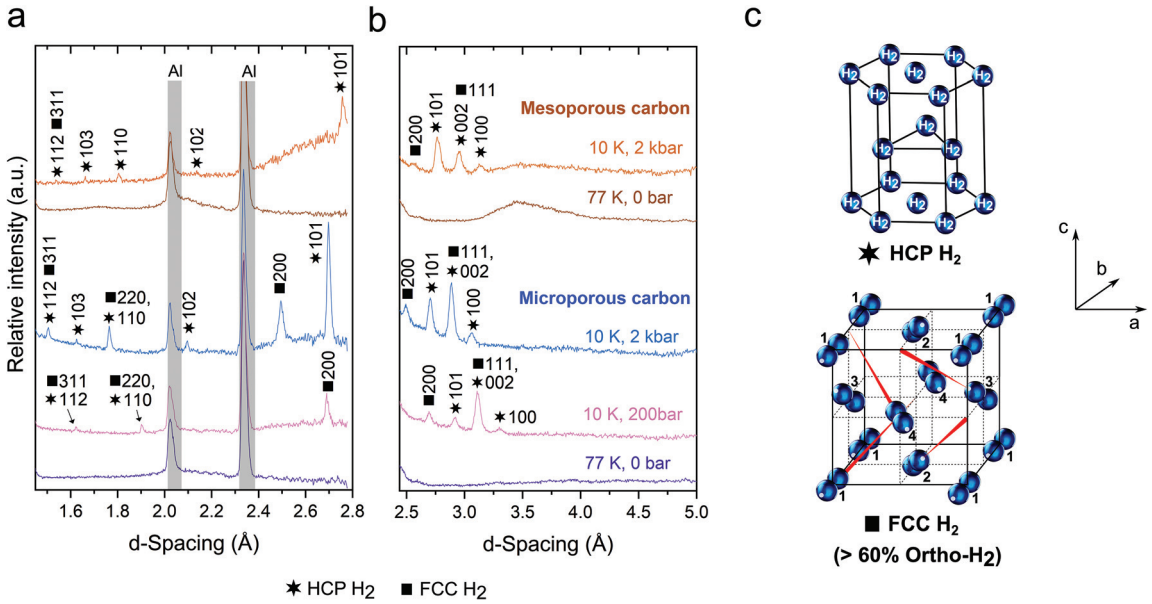

Fig. 1 Neutron powder diffraction of confined crystalline H_2 at low temperature. Diffraction data from (a) detector Bank 5 and (b) Bank 3 of the GEM diffractometer for microporous TE7 and mesoporous OLC carbons under vacuum (0 bar H_2) at 77 K and dosed with 200 or 2 kbar H_2 at 10 K. The Bragg peaks reveal the presence of two distinct crystalline phases of H_2 (HCP ★ and FCC ■) in the porous carbons at 10 K. Reflections from the aluminium sample holder are shaded in grey and patterns are offset in the *y*-direction, for clarity. (c) H_2 crystal structures for the orientationally disordered HCP H_2 lattice and the orientationally ordered FCC H_2 lattice.[12]

2.6 Scanning transmission electron microscopy energy dispersive X-ray (STEM-EDX)

Ground samples were dispersed in ethanol and dropped onto copper TEM grids and left to dry. Grids were analyzed on a JEOL JEM-2100F for STEM-EDX analysis.

2.7 Inductively coupled plasma optical emission spectroscopy (ICP-OES)

To analyze the trace metal content, samples were first digested in Piranha acid solution ($3H_2SO_4 : H_2O_2$) at 2 mg ml^{-1}. The sample was gently heated up to 80 °C to aid digestion and then to 290 °C to near-complete evaporation. The samples were then diluted in 10 mL of 1% HNO_3 solution and filtered through a 0.22 μm filter. Samples were analyzed for trace metals against a calibration standard using an Agilent 710 ICP-OES. Each metal was referenced using at least three optical emission wavelengths.

3. Results and discussion

3.1 Identification of the crystalline arrangement of the confined H_2 phases

To evaluate the effects of nanoscale confinement on the crystal structures and phase diagram of H_2, hydrogen sorption in two well-characterized amorphous, activated carbons (a microporous "TE7" activated carbon and a mesoporous onion-like carbon "OLC") was investigated. Both materials contain slit-shaped pores[24,26] exhibiting homogenous graphitic carbon adsorption surfaces with few surface oxygen groups[16] and present comparable total pore volumes between 0.8–0.9 cm^3 g^{-1}, as determined from gas sorption analysis (see ESI – Table S1†). The different pore diameters of the two activated carbons made them ideal candidates for evaluating the effect of nanoscale confinement of H_2 on the stability of the solid phases of confined H_2. Highly microporous carbons like TE7 have been shown to cause extreme densification of H_2 at temperatures ~77 K due to their sub-nanometre pores.[15,16,22] Mesoporous carbons like OLC show lower levels of H_2 densification, owing to larger pore diameters.[15,16] The TE7 used in this study exhibits a modal pore size of 0.55 nm with only a small proportion of mesopores (see ESI – Fig. S1†). OLC, the mesoporous activated carbon control, had a modal pore size of 9.5 nm and negligible microporosity in the pore diameter range <1 nm. Examination of the effects of nanoconfinement on the structural arrangement of H_2 forming within the pores was conducted at selected pressures and temperatures using "normal-H_2" on the GEM neutron diffraction instrument, at the ISIS neutron source, Rutherford-Appleton Laboratories. Neutron diffraction data was collected for both TE7 (microporous) and OLC (mesoporous) carbons under vacuum at 77 K and with adsorbed H_2 at 10 K (where bulk solid H_2 is known to form[14]) and at pressures of 200 bar and 2 kbar (where the pore volume has reached saturation) (Fig. 1).

Upon dosing both TE7 and OLC porous carbons with H_2 at 77 K, cooling to 10 K, and data collection over 2–3 h, sharp diffraction peaks originating from crystalline solid H_2 emerged (Fig. 1). To the authors' knowledge, this represents the first observation of crystalline H_2 nanoconfined in the pores of activated carbons.[27] Diffraction patterns were indexed (Table S2†),

revealing phase I solid H_2 ($P6_3/mmc$ HCP) was present in the pores, as might be expected for bulk H_2 at these temperatures and pressures.[5,12] However, clear diffraction peaks consistent with a $Pa3$ FCC H_2 crystal packing system were also observed to be present in the microporous TE7, with trace amounts of FCC H_2 also seen for the OLC material at 2 kbar. FCC H_2 is a metastable and orientationally-ordered phase, requiring the *ortho*-H_2 concentration to be >60% and the alignment of *ortho*-H_2 electric quadrupoles,[11,28] indicating a high concentration of *ortho*-H_2 was present in the microporous carbon at low temperatures and that thermodynamic *ortho-to-para* conversion of confined H_2 did not reach the 10 K equilibrium composition ratio (99.8% *para*-H_2).[12] Integration of the area under the diffraction peaks revealed the relative proportion of FCC : HCP was significantly higher in microporous carbon than in mesoporous carbons (see Table S3†), indicating that the sub-nanometre pores of TE7 may favour the formation of the FCC phase.

In addition to this, observation of multiple peaks consistent with the FCC *ortho*-H_2 phase at these temperatures is highly significant, as bulk FCC *ortho*-H_2 typically only forms below ~3 K and 5 K at 200 bar and 2000 bar, respectively.[12] FCC H_2 has not been previously observed in confined systems, with prior neutron diffraction measurements of H_2 confined in mesoporous (7 nm pore diameter) Vycor glasses showing only the HCP phase at 2 K (ref. 29) or only short-range order in mesoporous carbons.[27] To gain further insight into the thermal stability of the observed H_2 phases confined in the porous carbons, the temperature and pressure dependence of the observed crystalline phases was studied. For comparison, a summary of the confined phases observed in microporous TE7 across the examined temperatures and pressures is contrasted to the bulk H_2 phase diagram[12] (Fig. 2).

At 200 bar, the FCC phase disappeared by 15 K (Fig. 2a & S3†) but at 2 kbar was observed up to a temperature of 25 K (Fig. 2b & S4†), approximately five times higher than achievable in the bulk. However, the ratio of FCC : HCP also decreased with increasing pressure, from 4.7 : 1 to 1.2 : 1 (at 10 K). The increased thermal stability of the FCC *ortho*-H_2 phase suggests that *ortho*-H_2 in the subnanometre pores of TE7 may be strongly bound, aiding the molecular ordering of the FCC phase and enhancing the binding energy in the *ortho*-H_2 crystal lattice.[30] In contrast, within the range of temperatures and pressures explored, the confined HCP phase appeared to follow the bulk phase diagram, with no crystalline phase observed above the bulk solid/liquid phase boundary (Fig. 2). However, small shifts to this phase boundary may be uncovered with mapping over finer temperature increments.

A broad shoulder appeared in the *d*-spacing region of 2.6–3.6 Å in detector bank 3, with a corresponding broad peak in detector bank 5, centred at 2.6 Å and persisting for temperatures up to 77 K (Fig. S3 and S4†) suggesting possible short-range order or a glassy state. A glassy solid with the same intermolecular spacing was also observed for H_2 confined in a zeolite at very high pressures.[31] However, a comparison between changes in momentum transfer (Q) in both diffraction banks 3 & 5 did not show a match in background oscillations (Fig. S7†), therefore, this broad peak is likely due to an incoherent scattering effect than diffuse scattering caused by H_2 with short-range order.

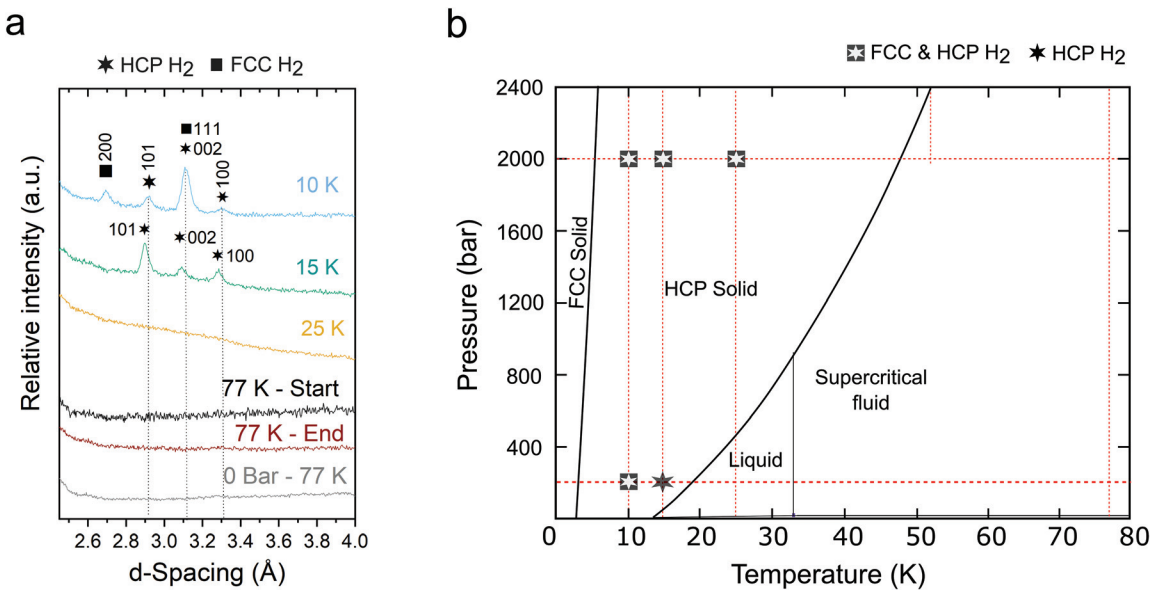

Fig. 2 Temperature and pressure dependence of the confined crystalline phases in microporous carbon. (a) Temperature-dependent neutron powder diffraction data of microporous TE7 dosed to 200 bar H_2 at 77 K (detector bank 3) showing the disappearance of the FCC phase at 15 K and loss of long-range order at 25 K. Dotted lines are added as a guide to the eye and patterns are offset in the *y*-direction for clarity. (b) Bulk phase diagram of *ortho*-H_2 at T = 0 as a function of pressure overlaid with the observed crystalline phases of H_2 in microporous TE7 in this experiment. Red lines represent the experimental pressures and temperatures observed *via* neutron diffraction.

To determine the effect of confinement on the size of the unit cell, the unit cell parameters were calculated by Rietveld refinement (Table S4†). Notably, the temperature dependence of the unit cell dimensions for HCP H_2 was found to differ at the two pressures studied. At the lower H_2 pressure, (200 bar) negative thermal expansion was observed (Fig. S3†). As the temperature decreased from 15 to 10 K, the HCP unit cell expanded *via* elongation of the *c*-axis, leading to a deviation of the *c*/*a* ratio from the ideal value (Table S4†), suggesting that the molecular H_2 is becoming anisotropic, as expected for ordered *ortho*-H_2.[12] In contrast, at the higher pressure studied (2 kbar), the unit cell exhibited negligible thermal expansion. The negative thermal expansion of the confined HCP phase at 10 K, 200 bar may be related to an incomplete HCP–FCC phase transition occurring at this temperature and pressure, with structural transitions from HCP to FCC typically accompanied by an expansion of volume.[32,33] This deviation may be due to strain induced by the nanoconfinement or too low a local concentration of *ortho*-H_2 required for FCC. In comparing the molar volume of the confined phases in the two activated carbons, both HCP and FCC were 7% larger in OLC than in TE7 at comparable pressures indicating that a higher density is achieved in smaller pores, consistent with previous calculations and gas sorption measurements.[15,16,20] However, the molar volumes of the nanoconfined crystalline phases appeared to be larger than the bulk solids at similar temperatures and pressures[11,13,34] (see Table S5†). Similarly, for H_2 confined in a zeolite material at high pressures,[31] a larger intermolecular separation than the bulk equivalent was also observed.

With no evidence for a crystalline solid phase at 77 K and larger unit cell volumes of confined crystalline phases, when compared to the bulk, the neutron diffraction suggests that previous reports of high-density solid H_2 above the critical temperature[15,16,20,21] are likely to be a high-density amorphous/glassy phase. However, previous reports were conducted at lower pressures than used in this study; thus further neutron diffraction experiments across 1–200 bar will be required to understand the confined phase diagram and confirm if the FCC phase can be observed above the critical temperature.[22]

3.2 Effect of H_2 adsorption environments in microporous carbon

To understand how the adsorption environments in TE7 cause the formation of FCC *ortho*-H_2 and increase its thermal stability, the effects of nanoconfinement on the rotational dynamics and distribution of both *para* and *ortho*-H_2 adsorbed in microporous carbon TE7 was examined by temperature-dependent INS using the IN4C spectrometer at the Institute Laue Langevin, Grenoble. The carbon was dosed with 1 bar high purity (99.999%) normal H_2 at 77 K to saturate the pores, subsequently cooled to temperatures between 40 and 4 K, and a detailed analysis of the rotations *via* INS was conducted (Fig. 3a–d and Table S6†).

In bulk H_2, the transition energy between the first nuclear rotational levels is 14.7 meV. Because H_2 is a quantum solid, this is observed as a singular rotor peak in the INS[16,17] and indicative of translationally pinned (hence solid-like) and freely rotating H_2 – see peak (1) in Fig. 3a–d. However, upon adsorption, interaction with an anisotropic electrostatic field can hinder the free rotation of the H_2 molecule and result in a lowering of rotational energy and the splitting of the rotational transition peak.[18,35–37] In porous graphitic carbon, as the pore width narrows to <1 nm,[38] the overlap of the anisotropic potential from pore walls is significant enough to hinder the free rotation of H_2 and alter the rotational energy levels, lifting the degeneracy of the triplet $J = 1$ state and causing a 2 : 1 split in the magnetic rotational sub-levels (m) as shown in Fig. 3e.[36,39,40] The ordering of the split states depends upon the negative or positive interaction of electrostatic adsorption potential with the molecular orientation of the rotations of H_2. Thus, the rotational energies of a parallel and perpendicular alignment of H_2 to the pore surfaces differ.[39,41] Furthermore, as the pore width decreases, the overlapping anisotropic potential from the graphitic pore walls increases, further separating the rotational potential energy of each orientation and increasing the magnitude of the energy gap (Δe) between the split states. These relationships have been clearly observed and demonstrated in previous studies of H_2 in slit-shaped pores of graphitic carbon.[18,36,38] In TE7, the sub-nanometre pore sizes are sufficiently small to fit up to a bilayer of H_2,[17,22] thus maximising the influence of overlapping anisotropic potential on the solid forming in the pores.

In the INS, two split peaks in a 2 : 1 intensity ratio for the $J = 0 \rightarrow 1$ excitation (labelled (2) in Fig. 3b & d) were observed, indicating *para*-H_2 confined in a micropore adsorption site <1 nm. For $J = 1 \rightarrow 0$, only the return transition from the lowest energy excited state to the ground state should be observed at low temperatures, due to the thermal population of states. Thus, peaks (2) & (3) in Fig. 3a and c appear to be from *ortho*-H_2 in two different micropore adsorption sites <1 nm and not freely rotating *ortho*-H_2. The peak at −13 meV is mirrored in the INS neutron energy loss spectra, hence this peak represents *ortho*-H_2 adsorbed at the same micropore site as *para*-H_2: site (2). The peak at −8 meV likely represents *ortho*-H_2 confined in a much higher anisotropic potential causing an increased Δe, such as an even smaller pore[36,38] – designated micropore site (3). Note that it is unlikely that the peak labelled (3) represents a phonon mode, as it is not observed in the neutron energy loss spectra and is too high energy for a quantum translation. Furthermore, peak (3) is unlikely to be the result of a metal impurity phase in the carbon as both EDXA and ICP-OES of samples reveal negligible trace metal content and no residual chlorine after acid washing, confirming the purity of the sample (see ESI – Fig. S8 and Table S7†). Paramagnetic metal centers are also known to rapidly catalyse *ortho*-to-*para* conversion.[12,42] Hence, the presence of significant metal impurities would preclude the observation of significant proportions of *ortho*-H_2 at this site and hence transitions in the neutron energy gain spectra would not be

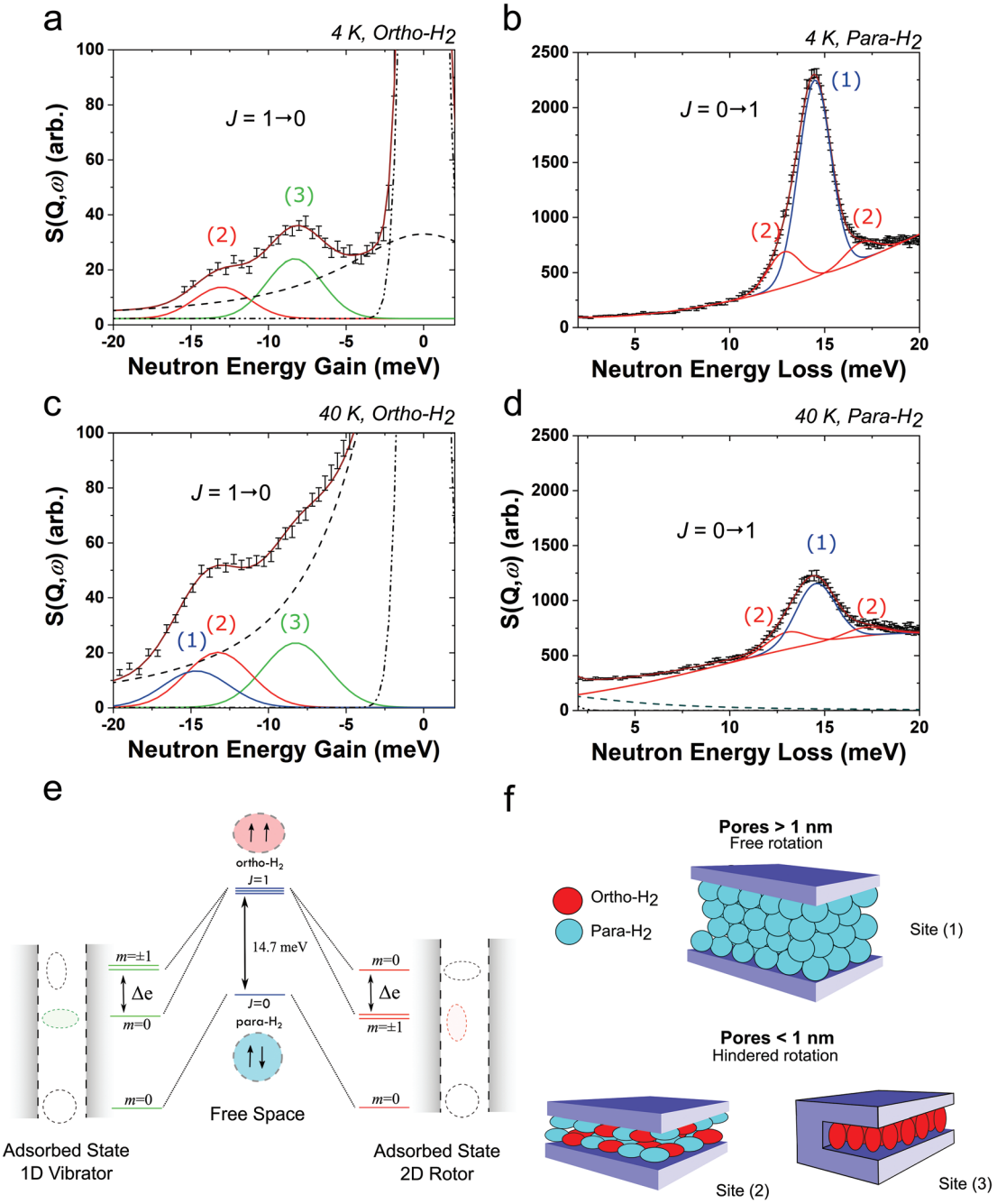

Fig. 3 Nanoconfinement effects on the quantum rotations of adsorbed *ortho* and *para*-H_2. Temperature-dependent INS of $J = 1 \rightarrow 0$ *ortho*-to-*para* and $J = 0 \rightarrow 1$ *para*-to-*ortho* transitions of 1 bar H_2 confined in highly microporous TE7 at 4 K (a, b) and 40 K (c, d), $Q = 3.4$ Å^{-1}. A background spectrum of the carbon under vacuum was recorded at each temperature before dosing H_2 and subtracted from the raw data. Peak contributions to the rotational transition are shown in solid lines, freely rotating H_2 in pores >1 nm are labelled (1), rotationally hindered H_2 in pores <1 nm are labelled (2) and (3). Dashed lines represent contributions to the elastic scattering peak. (e) Quantum rotational levels of H_2 in free space and adsorbed in a pore with a strong anisotropic potential causing 1D or 2D rotation. Adsorption into the pore lifts the degeneracy of $J = 1$ and splits the magnetic rotational sub levels. (f) Distribution of *para*- and *ortho*-H_2 across the three different adsorption sites in TE7 at 4 K, displaying the dominant molecular rotational orientation.

observed by 4 K.[42–44] Finally, if a metal centre were present (magnetic or non-magnetic), an analogous peak in the neutron energy loss spectra would be observed.[37,43,45–47] Here no such peak is observed.

The approximate distribution of the adsorption sites and *ortho*/*para*-H_2 was inferred at 4 K (where all H_2 is solid) by comparing the peak areas of the split and unsplit peaks from adsorbed *ortho* ($J = 1 \rightarrow 0$) and *para* ($J = 0 \rightarrow 1$) transitions,

allowing percentages of *ortho*/*para*-H_2 to be calculated at each site (Table S8†). Accounting for the difference in spin-dependent incoherent scattering cross-sections,[48] 31% of total adsorbed H_2 exhibited split rotational peaks (2,3) indicating a barrier to rotation from the strongly anisotropic potential in the pores <1 nm. The remaining contribution came from the single peak at 14.5 meV (1), *i.e.* freely rotating H_2, likely originating from the multiple layers of H_2 in pores >1 nm and unaffected by high anisotropic potential.[35] The distribution is in good agreement with the total pore volume distribution observed by gas sorption (Fig. S1†). The peaks and splitting observed in the INS are thus consistent with three types of adsorption environment within the carbon affecting H_2, one mesopore-type environment >1 nm diameter, site (1), and two different micropore environments <1 nm (sites (2) & (3)), causing substantial perturbation to H_2 rotations through nanoconfinement – see Fig. 3f.

3.3 Preferential stabilisation of H_2 spin isomers *via* loss of rotational freedom

As well as the observed differences in the molecular ordering, significant differences in the *para* : *ortho* ratio could be found for the different adsorption locations in the carbon, exposing a variation in the thermodynamic conversion of *ortho-to-para* for the different pore sizes (Fig. S9†). An illustration of the distribution of *ortho*/*para*-H_2 throughout microporous carbon at 4 K is displayed in Fig. 3f. At 40 K, both freely rotating *para* and *ortho*-H_2 (87 : 13) are observed in mesopore adsorption site (1), but by 4 K only freely rotating *para*-H_2 is observed, indicating rapid and complete thermodynamic conversion of *ortho-to-para* has occurred in pores >1 nm. Such behaviour has also been observed for activated charcoals, used for catalytic conversion of *ortho*-H_2.[39] An increased number of nearest neighbour hydrogen molecules (such as would be found in the layers of a filled mesopore) can drive intrinsic thermodynamic *ortho-to-para* conversion.[12] In contrast, for the micropore adsorption sites (2, 3), by 4 K, a 57 : 43 *para* : *ortho* ratio of contributions from adsorbed H_2 was observed, signifying the thermodynamic conversion of *ortho-to-para* in pores <1 nm is significantly lower than in pores >1 nm in activated carbons. Uniquely, at all temperatures, only $J = 1 \rightarrow 0$ transitions were observed from site (3), indicating only *ortho*-H_2 is adsorbed at this site. The results indicate preferential adsorption and potential spin trapping of *ortho*-H_2 down to low temperatures at site (3) (lower *ortho-to-para* thermodynamic conversion rate). This could be caused by the smallest pores in TE7 (~0.4 nm) or the disordered, amorphous nature of TE7 producing curvature or sites with three to four surrounding walls. Preferential adsorption of *ortho*-H_2 has been experimentally observed in other materials[41,49,50] and computationally demonstrated in the pores of carbon nanotubes up to 100 K.[51,52] In these studies, the generation of non-equilibrium mixtures of *ortho* : *para* H_2 was explained by the smaller energy gap between the first excited $J = 1$ rotational sub-level and ground state caused by the high anisotropic potential in nanoscale pores, observing greater spin selectivity in the smallest pores. As it is unlikely that metallic contaminants are the cause of site (3) due to the careful HCl pre-treatment of the porous carbon, these results demonstrate that subnanometre sized pores in activated carbon can also exhibit this preferential adsorption of *ortho*-H_2. Previous quasi-elastic neutron studies on a very similar highly microporous carbon[19] also show extreme confinement of H_2 in nanopores hinders the conversion of *ortho-to-para* H_2 as observed and described here.

To understand why particular sites seemed to favour higher concentrations of *ortho*-H_2, the potential barrier (V) to out-of-plane rotation from the adsorption sites and rotational constant (B) of confined H_2 was calculated by fitting the rotational energy levels to a double-well hindering adsorption potential[18] (see Experimental section). Micropore site (2) was consistent with a perturbed 3D rotator model[53] and exhibited a Δe of ~4 meV, corresponding to the estimated values $V = -10$ meV and $B = 7.1$ meV, thus promoting adsorption of H_2 molecules with their molecular axis oriented parallel to the surface. The potential barrier to rotation V is approximately two times larger than observed for other microporous carbons[18,54] and three times larger than that observed in carbon nanotubes[35,55] indicating that the H_2 is strongly confined in the anisotropic environment of these micropore sites. For micropore site (3), two scenarios are possible: (i) almost free 2D rotations originating from a (J, m) = (1, ±1) → (0, 0) transition, which can occur for strongly attractive potential surfaces with $V \sim -150$ meV and $B = 7.1$ meV or (ii) severely restricted rotations fitting the '1D vibrator' model with the H_2 molecular axis oriented perpendicular to the surface[41]originating from a (J, m) = (1, 0) → (0, 0) transition, with a repulsive anisotropic potential of $V \sim 30$ meV and $B = 7.35$ meV. Due to the low thermal population of states, the higher energy transition of the split states is not expected to be observed for adsorbed *ortho*-H_2, however, these are projected to occur at −55 meV and −21 meV, for scenarios (i) and (ii), respectively. Examining the neutron energy gain spectrum (see ESI – Fig. S10†), a small contribution is observed at −23 meV, very close to that calculated for scenario (ii), indicating a 1D vibrator model at site (3) out of thermal equilibrium. Given both the extremely high interaction potential barrier for scenario (i), and the possible observation of the higher energy split state of scenario (ii), scenario (ii) seems much more probable in the framework of H_2 physisorption in a system out of thermodynamic equilibrium. This type of anisotropic potential has not been observed in carbons previously and is more commonly observed for *ortho*-enrichment surfaces.[41] However, in all previous INS studies of H_2 in porous carbons the neutron energy gain spectrum has not been analysed in detail[16–18,22,35,36,38,42,48,55–57] and therefore may have overlooked the existence of preferentially adsorbing sites with high anisotropic potential caused by extreme confinement. These data are also consistent with previous computational studies that indicate increased potential barrier in nanoscales pores generate greater spin selectivity and produce non-equilibrium mixtures of *ortho* : *para* H_2 in carbonaceous materials.[51,52] Additionally, the calculated mean squared displacement $\langle U^2 \rangle$

of H_2 (Table S6 and Fig. S6†) is significantly lower at site (3) than site (2) and (1) by ~17% and 29% respectively, indicating a smaller delocalization in space – validating stronger confinement, adsorption and perturbed rotation at site (3).

3.4 Effects of nanoscale confinement on stabilization of H_2 phases

Considering the relationship of these observed confinement effects to the observed changes to phase behaviour, a greater understanding of why the observed crystalline phases form can be obtained. The decreased thermodynamic conversion of *ortho*-to-*para* in pores <1 nm, preferential adsorption, and spin trapping of *ortho*-H_2 at site (3) observed *via* INS correlate well with the increased proportion of molecularly ordered FCC *ortho*-H_2 found in microporous carbons *via* neutron diffraction. Likewise, the high level of thermodynamic conversion of *ortho*-to-*para* observed in pores >1 nm observed *via* INS correlates with the lower proportion of the FCC phase and majority HCP phase found in mesoporous carbons. Additionally, the increase in unit cell volume could be related to a small increase in H–H bond length. In site (2), the most widespread micropore site, the calculated rotational constant of H_2 deviated from normal, suggesting an elongation to the bond length by ~+2%. In turn, this could cause an increase in molar volume by ~6%, similar to what was observed *via* diffraction (Table S5†). Previous INS studies have also estimated elongation up to 7% for H_2 confined in single-walled carbon nanotubes (10, 10).[35] However, as bond elongation is dependent on the polarization of the H_2 molecule (for example, from an increased level of anisotropic potential such as that found in subnanometre pores) this explanation does not account for the greater increase in molar volume observed in mesoporous carbon, and thus requires further study.

Regarding the increase in thermal stability of the FCC *ortho*-H_2 phase confined in microporous carbon, similar changes to phase behaviour has been observed for other small molecules confined in nanoscale pores and have been shown to be related to both the pore size and the ratio of absorbate–substrate : absorbate–absorbate interactions.[58–60] In these cases, stronger adsorbate–substrate interactions in nanoscale pores increase the thermal stability of the confined solid[61–64] and stronger adsorbate–adsorbate interactions in nanoscale pores reduce the phase transition temperature.[64,65] Here we posit that the same mechanism is in play, where substrate–absorbate interactions are greater than absorbate–adsorbate interactions, lowering the total internal energy of the confined crystal with respect to the bulk phase and inducing molecular order in the confined phase at higher temperatures. This can be understood by first comparing the bulk to confined phase FCC *ortho*-H_2 and observing changes to the rotational spectrum. For bulk H_2, the lowest energy crystal confirmation for high *ortho*-H_2 concentrations is the FCC phase.[12,66] In the HCP phase, the molecules are free to rotate in free space (Fig. 1C), making it a higher energy, molecularly disordered quantum solid. In the FCC phase, the electric quadrupoles (EQQ) of the *ortho*-H_2 molecules orient themselves to lower interaction energy (Fig. 1C), reducing the rotational degrees of freedom of the molecules and reducing the total internal energy of the solid[12,67,68] resulting in a molecularly ordered solid. The reduction in energy from EQQ coupling between molecules can be considered the 'binding energy' of the FCC phase. This binding energy can be correlated to a drop in the rotational energy across the bulk HCP–FCC transition for various concentrations of *ortho*-H_2.[28,30] As the concentration of *ortho*-H_2 increases in the solid, the observed binding energy in the solid also increases. Consequently, increasing EQQ coupling in the solid raises the HCP–FCC transition temperature in tandem.[69] However, even for a 100% *ortho*-H_2 solid, the average increase in the binding energy of an *ortho* molecule to all other *ortho* molecules in bulk FCC solid is particularly low (~0.3 meV (ref. 28 and 30)) and explains why there is such a low transition temperature in the bulk (temperature easily overcomes the binding energy and disorders the molecules). Thus, the adsorbate–adsorbate interaction is very weak for solid H_2 compared to the interaction energy between adsorbate–substrate of H_2 adsorbed to a surface or confined in a pore. Interestingly, changes to rotations and internal energy upon the bulk HCP–FCC transition, are strikingly similar to the changes observed for *ortho*-H_2 upon adsorption/confinement in highly anisotropic potential. As described previously, the binding strength to the interface can be strong enough that the free rotation of H_2, which usually persists even in the solid-state, is hindered, accompanied by loss of degrees of rotational freedom and a loss of rotational energy in the process. The stronger the binding, the more significant a perturbation to the rotational energy.[70] It is known that *ortho*-H_2 typically binds more strongly to the substrate than *para*-H_2[52,70–74] due to the electrostatic interaction of the substrate with the electric quadrupoles of *ortho*-H_2 causing preferred orientation or imposed molecular ordering of *ortho*-H_2 on the surface, lowering its rotational energy and increasing its overall binding strength to the substrate. This is demonstrated by higher desorption temperatures/enthalpies of adsorption for the *ortho* species,[70,72,74] and loss of rotational degrees of freedom upon adsorption or confinement.

For a nanopore of dimensions allowing up to 2 layers of H_2, the effect on the confined phase is maximised. Here the strong adsorbate–substrate interactions facilitate the molecular ordering required for the low energy FCC phase even at high temperatures by lifting the degeneracy of the $J = 1$ state and altering the rotational degrees of freedom (Fig. 3c). The strong binding to the surface lowers the rotational energy of all the molecules (Fig. 3e) and hence total internal energy of the confined, 2-layer solid is reduced compared to the bulk equivalent, thus increasing the thermal stability of the FCC phase when confined. This can be semi-quantitatively observed in the changes to the rotational energy spectrum. In the micropores of TE7, the rotational energy of confined *ortho*-H_2 was observed at 13.3 meV and 8 meV as compared to 13.7 meV for bulk FCC *ortho*-H_2[28,30] indicating the confined *ortho*-H_2 is in a lower rotational energy state than the bulk. Likewise, the calculated potential barriers to rotation in the confined phase are much

higher than the EQQ coupling binding energy observed and calculated in the bulk phase.[28,30,68,75]

With this understanding of how confinement can affect the phase behaviour of H_2, the thermal stability of the confined phase could theoretically be increased further. If other materials that exhibit preferential adsorption, high enthalpies of adsorption and significant perturbations to the rotational degrees of freedom of H_2, can be engineered to have subnanometre pores similar to those shown in activated carbons, the overlap of anisotropic potential will be much greater and enhance the confinement effects, increasing the proportion and thermal stability of confined FCC *ortho*-H_2 higher than observed here. Temperature-dependent structural studies and rotational dynamics studies of H_2 confined in sub-nanometre pores of materials such as Al_2O_3 or BN would be recommended to test the theory.

The pore geometry may also have an influence on the thermal stability of the confined phase. In porous carbons, the degree of rotational splitting is greater for slit-like pores when compared to cylindrical,[18,35,54,55] likewise, calculated densities of confined H_2 are also higher[17] indicating slit-shaped pores may exhibit a greater enhancement to the thermal stability of FCC *ortho*-H_2. However, the effects could differ in other material compositions with surface inhomogeneities and require further study.

4. Conclusions

Through judicious evaluation of the structural and dynamical properties of H_2 confined in porous activated carbons, we have demonstrated that the thermal stability of known crystalline phases of H_2 can be enhanced by nanoconfinement to enable departures from the phase diagram of bulk H_2. We show adsorbed H_2 is distributed across three adsorption environments in the TE7 activated carbon, indicating two micropore sites <1 nm with high potential barriers perturbing the rotations of H_2 and a third mesopore site >1 nm with close-to-free rotation, correlating well with the differential pore volume distribution. Uniquely, microporous site (3), believed to correspond to the smallest pores found in the TE7 activated carbon, causes preferential adsorption of *ortho*-H_2 and perpendicular orientation of molecules to the pore surface, which is best described by the 1D vibrator model. The severe restriction of rotation at site (3) also results in a reduced thermodynamic conversion rate from *ortho-to-para*, resulting in spin trapping down to low temperatures.

For the first time, neutron diffraction also revealed that both HCP solid H_2 and FCC solid *ortho*-H_2 were present inside both microporous and mesoporous carbon, with a higher FCC : HCP ratio found in microporous carbon and a much lower ratio in mesoporous carbon. The increased proportion of metastable orientationally ordered FCC correlates to the preferentially adsorbed and spin-trapped *ortho*-H_2 found in micropore site (3) as well as the reduced thermodynamic conversion found in pores <1 nm found by INS. Importantly, we discovered that nanoconfinement of H_2 significantly increases the structural transition temperature of FCC to HCP H_2 up to five times higher than is seen in the bulk at 2 kbar. The increased thermal stability of the orientationally ordered FCC *ortho*-H_2 phase is linked to the high potential barrier to rotation observed in micropore sites, aiding molecular ordering of the molecules, increasing the binding energy of the crystal lattice and lowering the total internal energy of the confined solid with respect to the bulk equivalent. In contrast, the HCP phase followed the expected bulk liquid/solid transition. Calculated unit cells of confined H_2 revealed that the unit cell volumes of the adsorbed H_2 are smaller in microporous carbon than in mesoporous carbon, but larger than that of bulk H_2 at comparable temperatures and pressures. We also determine that above the bulk HCP solid/liquid phase boundary, the H_2 may display solid-like properties, but no crystalline phases are observed at the pressures and temperature examined. Further neutron diffraction experiments across 1–200 bar would be useful to understand the confined phase diagram and confirm if the FCC phase can be observed above the critical temperature.

The findings reported here demonstrate how the unique interactions of nanoconstrained spaces with *para* and *ortho*-H_2 can allow manipulation of the phase diagram. The results present new insight into how materials could be engineered for interactions with individual nuclear spin isomers of H_2 to improve temperature stability in hydrogen sorbent systems and applications that require compact and condensed phases of H_2. Further alteration of hydrogen's rotational energy levels by an increasingly anisotropic potential in nanoconfined spaces may allow us to manipulate the phase diagram further or achieve other exotic non-equilibrium solid phases of interest to condensed matter physics or hydrogen storage research at more amenable temperatures and pressures.

Conflicts of interest

There are no conflicts of interest to declare.

Acknowledgements

The authors thank the US Army Research Office for funding this project (W911NF-19-1-0321-P00001) and the UK Engineering and Physical Sciences Research Council (EPSRC) for an EPSRC Research Fellowship for VPT (EP/R01650X/1). The authors thank the Science and Technology Facilities Council (STFC) for funding and allocation of ISIS beamtime (Proposal number RB1910448) and the Institut Laue Langevin for beamtime (Proposal number IN4C 7-05-468). Thanks also goes to Prof Steve Tennison and Tom Avery (MAST Carbon International) for providing the TE7 carbon beads and Volker Presser (INM, University of Saarbruken, Germany) for providing the OLC carbons, and to Rafael Balderas Xicohtencatl and Anibal J. Ramirez-Cuesta (Oak Ridge National Laboratories) for

useful discussions. VPT designed and managed the project and obtained the funding. LT and MT performed the materials characterization and testing. LT, VPT, and MT carried out the neutron experiments with the support of IdS, SR and SB. LT led the data analysis, with all authors contributing to data interpretation and the drafting of the manuscript.

References

1 S. van Renssen, *Nat. Clim. Change*, 2020, **10**, 799.
2 M. I. Eremets and I. a. Troyan, *Nat. Mater.*, 2011, **10**, 927.
3 R. P. Dias and I. F. Silvera, *Science*, 2017, **355**, 715.
4 P. Loubeyre, F. Occelli and P. Dumas, *Nature*, 2020, **577**, 631.
5 W. H. Keesom, D. E. Smedt and H. H. Mooy, *Commun. Phys. Libr. Leiden Univ.*, 1930, **19**, 814.
6 C. J. Pickard and R. J. Needs, *Nat. Phys.*, 2007, **3**, 473.
7 R. T. Howie, C. L. Guillaume, T. Scheler, A. F. Goncharov and E. Gregoryanz, *Phys. Rev. Lett.*, 2012, **108**, 125501.
8 P. Dalladay-Simpson, R. T. Howie and E. Gregoryanz, *Nature*, 2016, **529**, 63.
9 R. P. Dias, O. Noked and I. F. Silvera, *Phys. Rev. B*, 2019, **100**, 184112.
10 I. Goncharenko and P. Loubeyre, *Nature*, 2005, **435**, 1206.
11 A. F. Schuch, R. L. Mills and D. A. Depatie, *Phys. Rev.*, 1968, **165**, 1032.
12 I. Silvera, *Rev. Mod. Phys.*, 1980, **52**, 393.
13 R. L. Mills and A. F. Schuch, *Phys. Rev. Lett.*, 1965, **15**, 722.
14 B. A. Younglove, *J. Phys. Chem. Ref. Data*, 1982, **14**, 1.
15 N. C. Gallego, L. He, D. Saha, C. I. Contescu and Y. B. Melnichenko, *J. Am. Chem. Soc.*, 2011, **133**, 13794.
16 V. P. Ting, A. J. Ramirez-Cuesta, N. Bimbo, J. E. Sharpe, A. Noguera-Diaz, V. Presser, S. Rudic and T. J. Mays, *ACS Nano*, 2015, **9**, 8249.
17 M. Tian, M. J. Lennox, A. J. O'Malley, A. J. Porter, B. Krüner, S. Rudić, T. J. Mays, T. Düren, V. Presser, L. R. Terry, S. Rols, Y. Fang, Z. Dong, S. Rochat and V. P. Ting, *Carbon*, 2021, **173**, 968.
18 J. Bahadur, C. I. Contescu, A. J. Ramirez-Cuesta, E. Mamontov, N. C. Gallego, Y. Cheng, L. L. Daemen and Y. B. Melnichenko, *Carbon*, 2017, **117**, 383.
19 C. I. Contescu, D. Saha, N. C. Gallego, E. Mamontov, A. I. Kolesnikov and V. V. Bhat, *Carbon*, 2012, **50**, 1071.
20 J. E. Sharpe, N. Bimbo, V. P. Ting, A. D. Burrows, D. Jiang and T. J. Mays, *Adsorption*, 2013, **19**, 643.
21 L. He, Y. B. Melnichenko, N. C. Gallego, C. I. Contescu, J. Guo and J. Bahadur, *Carbon*, 2014, **80**, 82.
22 R. J. Olsen, A. K. Gillespie, C. I. Contescu, J. W. Taylor, P. Pfeifer and J. R. Morris, *ACS Nano*, 2017, **11**, 11617.
23 A. J. Ramirez-Cuesta, M. O. Jones and W. I. F. David, *Mater. Today*, 2009, **12**, 54.
24 M. Zeiger, N. Jäckel, M. Aslan, D. Weingarth and V. Presser, *Carbon*, 2015, **84**, 584.
25 W. G. Williams, R. M. Ibberson, P. Day and J. E. Enderby, *Physica B: Condens. Matter*, 1997, **241–243**, 234.
26 A. Hruzewicz-Kołodziejczyk, V. P. Ting, N. Bimbo and T. J. Mays, *Int. J. Hydrogen Energy*, 2012, **37**, 2728.
27 T. Roussel, R. J. M. Pellenq, M. Bienfait, C. Vix-Guterl, R. Gadiou, F. Béguin and M. Johnson, *Langmuir*, 2006, **22**, 4614.
28 H. Stein, H. Stiller and R. Stockmeyer, *J. Chem. Phys.*, 1972, **57**, 1726.
29 P. E. Sokol, R. T. Azuah, R. M. Gibbs and S. M. Bennington, *J. Low Temp. Phys.*, 1996, **103**, 23.
30 A. Bickermann, H. Spitzer, H. Stiller and R. Scherm, *Z. Phys. B: Condens. Matter Quanta*, 1978, **31**, 339.
31 W. Xu, X. Di Liu, M. Peña-Alvarez, H. C. Jiang, P. Dalladay-Simpson, B. Coasne, J. Haines, E. Gregoryanz and M. Santoro, *J. Phys. Chem. C*, 2021, **125**, 7511.
32 J. X. Yang, H. L. Zhao, H. R. Gong, M. Song and Q. Q. Ren, *Sci. Rep.*, 2018, **8**, 1.
33 B. Li, G. Qian, A. R. Oganov, S. E. Boulfelfel and R. Faller, *J. Chem. Phys.*, 2017, **146**, 214502.
34 A. Driessen and I. F. Silvera, *J. Low Temp. Phys.*, 1984, **54**, 361.
35 P. A. Georgiev, D. K. Ross, A. De Monte, U. Montaretto-Marullo, R. A. H. Edwards, A. J. Ramirez-Cuesta, M. A. Adams and D. Colognesi, *Carbon*, 2005, **43**, 895.
36 P. A. Georgiev, D. K. Ross, P. Albers and A. J. Ramirez-Cuesta, *Carbon*, 2006, **44**, 2724.
37 A. J. Ramirez-Cuesta, P. C. H. Mitchell, D. K. Ross, P. A. Georgiev, P. A. Anderson, H. W. Langmi and D. Book, *J. Mater. Chem.*, 2007, **17**, 2533.
38 R. J. Olsen, L. Firlej, B. Kuchta, H. Taub, P. Pfeifer and C. Wexler, *Carbon*, 2011, **49**, 1663.
39 K. Fukutani and T. Sugimoto, *Prog. Surf. Sci.*, 2013, **88**, 279.
40 D. White and E. N. Lassettre, *J. Chem. Phys.*, 1960, **32**, 72.
41 I. F. Silvera and M. Nielsen, *Phys. Rev. Lett.*, 1976, **37**, 1275.
42 C. M. Brown, T. Yildirim, D. A. Neumann, M. J. Heben, T. Gennett, A. C. Dillon, J. L. Alleman and J. E. Fischer, *Chem. Phys. Lett.*, 2000, **329**, 311.
43 P. D. C. Dietzel, P. A. Georgiev, J. Eckert, R. Blom, T. Strässle and T. Unruh, *Chem. Commun.*, 2010, **46**, 4962.
44 C. M. Brown, A. J. Ramirez-Cuesta, J. H. Her, P. S. Wheatley and R. E. Morris, *Chem. Phys.*, 2013, **427**, 3.
45 J. Z. Larese, T. Arnold, L. Frazier, R. J. Hinde and A. J. Ramirez-Cuesta, *Phys. Rev. Lett.*, 2008, **101**, 165302.
46 S. K. Callear, A. J. Ramirez-Cuesta, W. I. F. David, F. Millange and R. I. Walton, *Chem. Phys.*, 2013, **427**, 9.
47 A. J. Ramirez-Cuesta, P. C. H. Mitchell, D. K. Ross, P. A. Georgiev, P. A. Anderson, H. W. Langmi and D. Book, *J. Alloys Compd.*, 2007, **446–447**, 393.
48 S. Mamone, M. Jiménez-Ruiz, M. R. Johnson, S. Rols and A. J. Horsewill, *Phys. Chem. Chem. Phys.*, 2016, **18**, 29369.
49 T. R. Prisk, M. S. Bryan and P. E. Sokol, *Phys. Chem. Chem. Phys.*, 2014, **16**, 17560.
50 D. W. Brown, P. E. Sokol and S. A. Fitzgerald, *Phys. Rev. B: Condens. Matter Mater. Phys.*, 1999, **59**, 258.
51 T. Lu, E. M. Goldfield and S. K. Gray, *J. Phys. Chem. B*, 2006, **110**, 1742.

52 R. A. Trasca, M. K. Kostov and M. W. Cole, *Phys. Rev. B: Condens. Matter Mater. Phys.*, 2003, **67**, 1.
53 P. C. H. Mitchell, S. F. Parker, A. J. Ramirez-Cuesta and J. Tomkinson, *Vibrational Spectroscopy with Neutrons: With Applications in Chemistry, Biology, Materials Science and Catalysis*, World Scientific, Hackensack, NJ, 2005.
54 R. J. Olsen, M. Beckner, M. B. Stone, P. Pfeifer, C. Wexler and H. Taub, *Carbon*, 2013, **58**, 46.
55 F. Fernandez-Alonso, F. J. Bermejo, C. Cabrillo, R. O. Loutfy, V. Leon and M. L. Saboungi, *Phys. Rev. Lett.*, 2007, **98**, 2.
56 Y. Ren and D. L. Price, *Appl. Phys. Lett.*, 2001, **79**, 3684.
57 P. A. Georgiev, D. K. Ross, A. De Monte, U. Montaretto-Marullo, R. A. H. Edwards, A. J. Ramirez-Cuesta and D. Colognesi, *J. Phys.: Condens. Matter*, 2004, **16**, L73.
58 R. Radhakrishnan, K. E. Gubbins and M. Sliwinska-Bartkowiak, *J. Chem. Phys.*, 2002, **116**, 1147.
59 C. Alba-Simionesco, B. Coasne, G. Dosseh, G. Dudziak, K. E. Gubbins, R. Radhakrishnan and M. Sliwinska-Bartkowiak, *J. Phys.: Condens. Matter*, 2006, **18**, R15.
60 B. K. Peterson, J. P. R. B. Walton and K. E. Gubbins, *J. Chem. Soc., Faraday Trans. 2*, 1986, **82**, 1789.
61 K. Kaneko, A. Watanabe, T. Iiyama, R. Radhakrishan and K. E. Gubbins, *J. Phys. Chem. B*, 1999, **103**, 7062.
62 R. Radhakrishnan, K. E. Gubbins, A. Watanabe and K. Kaneko, *J. Chem. Phys.*, 1999, **111**, 9058.
63 A. Watanabe, T. Iiyama and K. Kaneko, *Chem. Phys. Lett.*, 1999, **305**, 71.
64 M. Sliwinska-Bartkowiak, G. Dudziak, R. Sikorski, R. Gras, K. E. Gubbins and R. Radhakrishnan, *Phys. Chem. Chem. Phys.*, 2001, **3**, 1179.
65 S. Gautam, A. I. Kolesnikov, G. Rother, S. Dai, Z.-A. Qiao and D. Cole, *J. Phys. Chem. A*, 2018, **122**, 6736.
66 N. S. Sullivan, *Can. J. Chem.*, 1988, **66**, 908.
67 N. S. Sullivan and R. V. Pound, *Phys. Rev. A*, 1972, **6**, 1102.
68 H. M. James and J. C. Raich, *Phys. Rev.*, 1967, **162**, 649.
69 R. L. Mills, A. F. Schuch and D. A. Depatie, *Phys. Rev. Lett.*, 1966, **17**, 1131.
70 A. Van Itterbeek, R. Hellemans and W. Van Dael, *Physica*, 1964, **30**, 324.
71 T. Sugimoto and K. Fukutani, *Phys. Rev. Lett.*, 2014, **112**, 1.
72 J. Heidberg, N. Gushanskaya and R. Schwarte, *Surf. Sci.*, 1995, **333**, 1473.
73 T. Magome, K. Fukutani and T. Okano, *J. Vac. Soc. Jpn.*, 1999, **42**, 286.
74 L. Amiaud, A. Momeni, F. Dulieu, J. H. Fillion, E. Matar and J. L. Lemaire, *Phys. Rev. Lett.*, 2008, **100**, 1.
75 A. B. Harris and A. J. Berlinsky, *Theoretical Analysis of Inelastic Neutron Scattering in Solid Hydrogen*, 1977.